RSC Advances

PAPER

View Article Online
View Journal | View Issue

Cite this: *RSC Adv.*, 2023, **13**, 15575

Tailoring the interfacial surfaces of tungsten and molybdenum tungsten disulfide electrodes for hybrid supercapacitors

Meshal Alzaid,*[a] Muhammad Zahir Iqbal,*[bc] Bandar Alqahtani,[a] Rakan Alanazi,[a] Ibrahim Hotan Alsohaimi,[d] W. S. Mohamed[a] and N. M. A. Hadia[a]

Received 8th February 2023
Accepted 28th April 2023

DOI: 10.1039/d3ra00847a

rsc.li/rsc-advances

The layered structures of tungsten disulfide (WS_2) and molybdenum tungsten disulfide ($MoWS_2$) are considered as the most promising electrode materials for energy storage devices. Herein, MS (magnetron sputtering) is required for the deposition of WS_2 and $MoWS_2$ on the surface of the current collector to attain an optimized layer thickness. The structural morphology and topological behavior of the sputtered material were examined *via* X-ray diffraction and atomic force microscopy. Three-electrode assembly was used to start the electrochemical investigations to identify the most optimal and effective sample among WS_2 and $MoWS_2$. CV (cyclic voltammetry), GCD (galvanostatic charging discharging), and EIS (electro-impedance spectroscopy) techniques were employed to analyze the samples. After preparing WS_2 with optimized thickness as the superior performing sample, a hybrid device was designed as WS_2//AC (activated carbon). With a remarkable cyclic stability of 97% after 3000 continuous cycles, the hybrid supercapacitor generated a maximum energy density (E_s) value of 42.5 W h kg^{-1} and 4250 W kg^{-1} of power density (P_s). Besides, the capacitive and diffusive contribution during the charge–discharge process and *b*-values were calculated by Dunn's model, which lay in the 0.5–1.0 range and the fabricated WS_2 hybrid device was found to have a hybrid nature. The outstanding outcomes of WS_2//AC make it suitable for future energy storage applications.

1. Introduction

The energy demand and supply has exploded exponentially during the last decade and now it is time to abandon fossil fuels. Renewable energy is going to be the major energy resource of the future; however, only its extraction would not suffice as there is a dire need for advance storage technologies for energy storage.[1,2] The two most important energy storage technologies now meeting the energy demands of the modern world are batteries and supercapacitors, but each come with its own merits and demerits. Battery storage technology is controlled by faradaic redox reactions occurring at the battery electrodes by means of which high energy density can be delivered.[3] Batteries, despite their promising features, face dendrite formation upon high power extraction as well as sluggish charge kinetics, which largely inhibit its high-power utilization.[4] In contrast, supercapacitors (SCs) of two types, *i.e.*, electric double layer capacitors (EDLCs) and pseudocapacitors retain the charges at the targeted electrode *via* electrostatic forces, which can be rapidly released when desired, thus catering to high power applications.[5] Although SCs are an integral component of numerous electronic devices but lack high specific energy, which is a crucial factor for an energy storage device.[6] Henceforth, the concept of merging the merits of both batteries and SCs can be realized employing both battery and capacitive grade electrodes into an individual device named as "supercapattery" or "hybrid supercapacitors".[7]

A hybrid device utilizes battery grade material for its anode and carbonaceous materials (graphene, CNTs, AC, *etc.*) as the negative terminal. The efficiency of electrochemical energy storage system is highly reliant on the electrode material utilized.[8] Thus, those materials with high porosity, large surface area, numerous redox active sites, and stable crystal structure are preferred.[9] Many materials are thoroughly investigated as electrode materials for hybrid supercapacitor applications including oxides, phosphides, phosphates, sulfides, and conducting polymers.[10–14] However, the low conductivity and stability of oxides, phosphates, and phosphides inhibit its practical implementations.[15] In contrast, transition metal sulfides (TMS) are an interesting contender material for energy

[a]*Department of Physics, College of Science, Jouf University, P.O. Box 2014, Al-Jouf, Sakaka, Saudi Arabia. E-mail: mmalzaid@ju.edu.sa*

[b]*Nanotechnology Research Laboratory, Faculty of Engineering Sciences, Ghulam Ishaq Khan Institute of Engineering Sciences and Technology, Topi, 23640, Khyber Pakhtunkhwa, Pakistan. E-mail: zahir@giki.edu.pk*

[c]*ZENTECH Research Laboratory, Faculty of Engineering Sciences, Ghulam Ishaq Khan Institute of Engineering Sciences and Technology, Topi, 23640, Khyber Pakhtunkhwa, Pakistan*

[d]*Department of Chemistry, College of Science, Jouf University, Al-Jouf, Sakaka, P.O. Box 2014, Saudi Arabia*

storage applications as they have unique electrochemical features. They have better charge storage capability and provide more redox active sites, thus leading to superior electrochemical performance.[16] TMS also has an enhanced electrical conductivity relative to oxides and are less electronegative, thus bringing flexibility to their use in various applications. Nandhini *et al.* synthesized NiS nanoparticles *via* hydrothermal approach for supercapacitor applications.[17] NiS possess a specific capacitance (C_s) of 964 F g^{-1} at a current density of 1 A g^{-1}. Multidimensional CoS/NiO architectures were utilized by Yang and coworkers as supercapacitor electrode materials. CoS/NiO provided a C_s of 1620 F g^{-1} at 1.0 A g^{-1} current density with a long-life cyclic stability.[18] Heydari *et al.* synthesized CuS nanohollow spheres for application in supercapacitors.[19] The synthesized material presented a maximum C_s of 948 F g^{-1} at 1 A g^{-1} current density. Transition metal dichalcogenides have also grabbed a significant position in the development of advanced energy storage devices due their layered 2D structure. Chen *et al.* reports graphene coupled with WS_2 for supercapacitor applications. The prepared sample displayed a maximum C_s of 383.6 F g^{-1}.[20] Mohan *et al.* synthesized WS_2 nanoflowers, whose fabricated symmetric supercapacitor delivers a C_s of 119 F g^{-1} at 1 A g^{-1}.[21] The stated literature highlights the importance of investigating sulfides for hybrid supercapacitor devices.

Herein, we analyzed the electrochemical response of tungsten di-sulfide (WS_2) and molybdenum-tungsten di-sulfide ($MoWS_2$) magnetron sputtered on nickel foam with distinct film thickness. 2D transition metal chalcogenides are fascinating materials in terms of their layered structure and electrochemical properties and hence structurally and electrochemically elucidated in this current work. All the prepared samples are first tested in the three-electrode cell setup and then the most optimized performing sample is combined with activated carbon (AC) to assemble a hybrid supercapacitor device, which showed decent energy and power densities. The theoretical approach is also applied to acquire an understanding into the charge storage mechanism of the fabricated device.

2. Experimental section

2.1. Deposition technique for WS_2 and $MoWS_2$

Numerous deposition methods can be used to produce WS_2 and $MoWS_2$ thin films. Through radio frequency sputtering (RFMS), we were able to create WS_2 and $MoWS_2$ thin films in this case. On NF substrate and glass slides, both $MoWS_2$ and WS_2 were sputtered using an Ollital multitarget RF-DC (sputtering apparatus) and using WS_2 and $MoWS_2$ targets procured from Stanford Advanced Materials. Quartz crystal was used to detect an *in situ* layer thickness by maintaining a substrate to a target distance of 60 mm. Also, the predeposition precautions were taken care of by maintaining a constant flow rate (50 SCCM) of Argon gas in the chamber along with plasma cleaning and presputtering of targets prior to deposition to eradicate any impurity present. For WS_2 and $MoWS_2$, separate samples totaling four were created. WS_2 samples were designated as W1, W2, W3, and W4 for film thicknesses of 150, 250, 350, and 550 nm, respectively. $MoWS_2$ was designated as M1, M2, M3, and M4 with film thicknesses of 217, 467, 733, and 1026 nm ± 4 nm, individually.

3. Results and discussion

3.1. Structural, microscopic, morphological, and surface analysis

The X-ray diffraction patterns of WS_2 and $MoWS_2$ are depicted in Fig. 1(a) and 2(a). The WS_2 X-ray diffraction pattern has significant high intensity diffraction peaks at 2θ of 28.92° (004), 39.32° (103), 43.48° (006), 49.16° (105), and 58.92° (008), respectively. These peaks are typical of tungsten disulfide, a substance having two unique structural phases, hexagonal and rhombohedral, which are completely consistent with one another and the ICDD database (PDF # 00-08-0237). In $MoWS_2$-amalgamated thin films, the higher significant peaks at 2θ values of 39.8° and 56.02° along with the planes (103) and (106), respectively, are linked with the $MoWS_2$ cubic structure ICDD database (PDF # 002-0132). Fig. 1(b) and 2(b) depict the Raman spectra of WS_2 and $MoWS_2$, respectively. The Raman spectrum of WS_2 features a second-order peak (2LA(M)) near the *M*-point of the Brillouin zone center, and both the material samples have first-order in-plane (E_{12g}) and out-of-plane (A_{1g}) optical peaks.[22] As shown in Fig. 1(c) and 2(c), SEM was adopted for analyzing the surface morphology of WS_2 and $MoWS_2$ layered over nickel foam (b). The SEM results at high-level magnification provides a clear explanation of the porous structure of substrate, which is completely coated in the sputtered material. In addition, EDX (energy dispersive X-ray spectroscopy) was carried out to perform an elemental assessment to determine the components of sputtered WS_2 and $MoWS_2$ on the substrate. The humps/peaks were checked for S, Mo, and W, which unquestionably proves that WS_2 and $MoWS_2$ exists on Ni-foam, as expressed in Fig. 1(d) and 2(d). Fig. 3(a)–(h) indicates the three-dimensional topology of the films described on the surface of glass slide, as measured by AFM for all the required samples.

3.2. Three-electrode electrochemical analysis

3.2.1. Cyclic voltammetry (CV). To start with the electrochemical analysis, three-electrode cell setup was assembled and cyclic voltammetry of the WS_2 and MoS_2 samples was performed in 1 M KOH electrolytic medium with Hg/HgO and platinum wire as the reference and counter electrodes, respectively. The CV of the WS_2 samples in Fig. 4(a)–(d) and $MoWS_2$ samples in Fig. 6(a)–(d) were noted at different scanning rates (3–50 mV s^{-1}) with 0–0.7 V scanning potential window. From the voltammograms of all the samples, it is clear that the samples possess battery grade nature as redox peaks are present at certain voltage values. The redox peaks indicate the existence of faradaic reactions, which in forward scan denotes oxidation reaction and in the negative scan shows reduction reactions.[23] The design of CV curves of all the samples is a mixture of EDLC and faradaic behavior, due to which the material has higher stability over increasing scan rates and has symmetric curves.

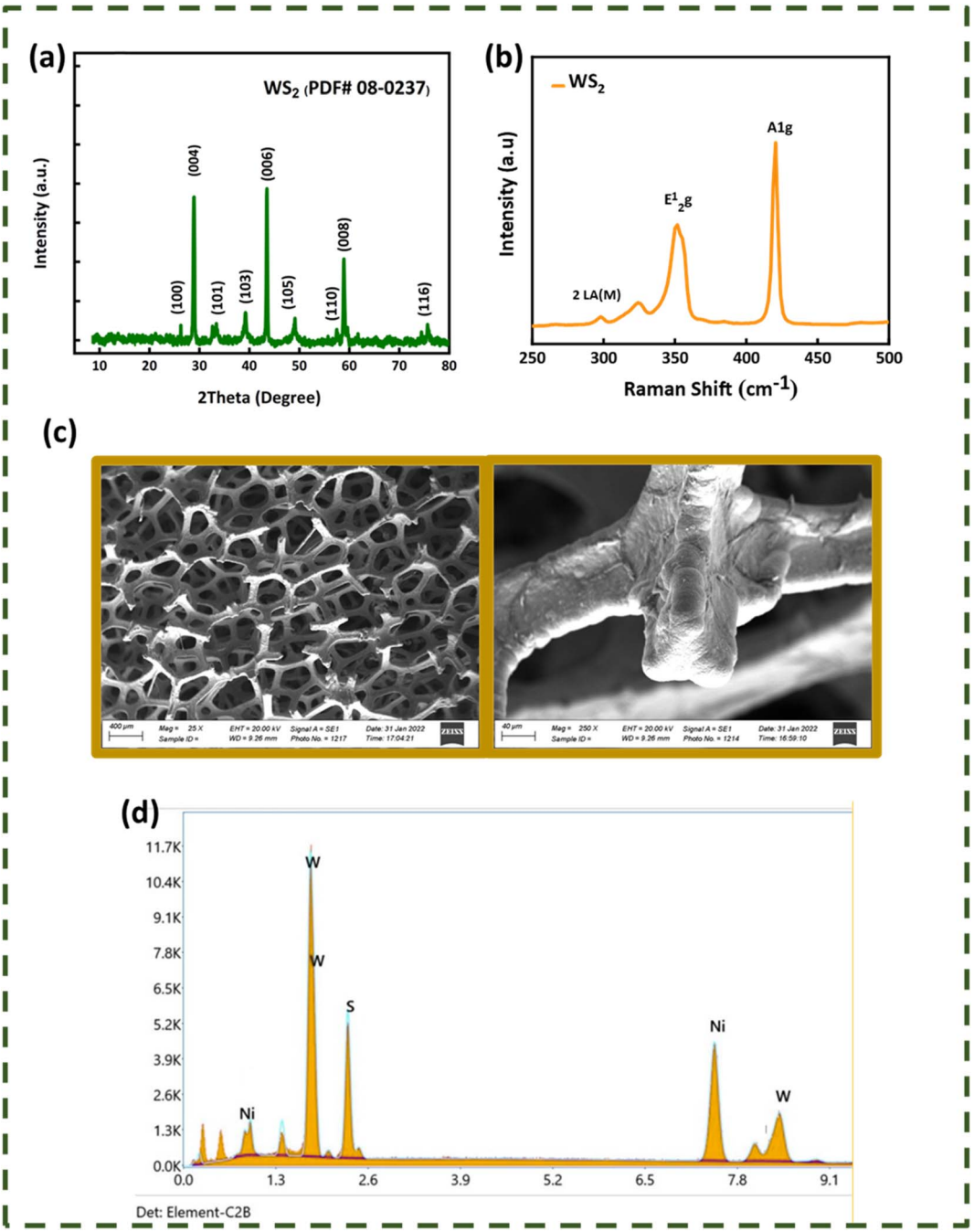

Fig. 1 (a) X-ray diffraction patterns of WS_2. (b) Raman spectrum of WS_2. (c) Scanning electron microscopy of magnetron-sputtered WS_2 on nickel foam. (d) EDX spectrum of WS_2.

An elevation in the peak currents can be observed at higher scan rates along with peak broadening, which means that the capacitive role is influential at higher scan rate values. This phenomenon is regarded to the availability of limited time for the ions to intercalate into the electrode; rather, they are adsorbed on the surface. For all the samples, a shift in the peaks toward higher potentials can also be observed, which is a characteristic of the battery-grade nature material. At the electrodes, the redox reactions may follow the following equations.

$$WS_2 + OH^- \rightarrow WS_2OH + e^- \quad (1)$$

$$MoS_2 + OH^- \rightarrow MoS_2OH + e^- \quad (2)$$

In case of WS_2, W2 has the largest peak currents and has larger area under the curve, which means that it has the highest specific capacity (Q_s) (Fig. 5(a)). Among different samples of $MoWS_2$, M3 covers the largest area under the curve, making it superior among others in term of charge storage, as can be seen

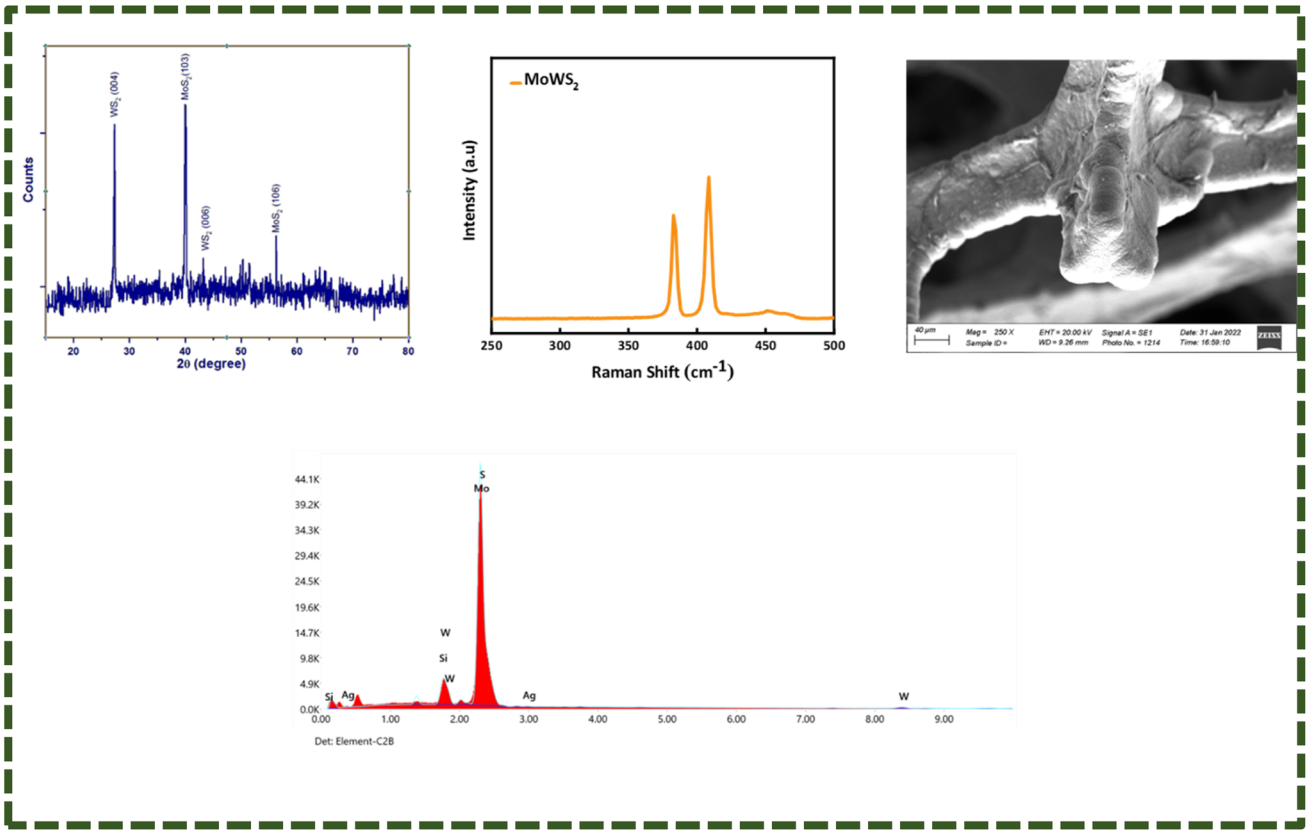

Fig. 2 (a) XRD patterns of $MoWS_2$. (b) Raman spectrum of $MoWS_2$. (c) SEM of magnetron-sputtered $MoWS_2$ on nickel foam, (d) EDX spectrum of $MoWS_2$.

in Fig. 7(a). Q_s can be calculated from the cyclic voltammograms using eqn (3) (ref. 24)

$$Q_S = \int \frac{I \times V \, dV}{2mv} \quad (3)$$

where '$\int I \times V \, dV$' is the area included under the CV curve, '' is the synthesized materials' mass, and 'v' is the scan rate. The specific capacities achieved from the cyclic curves at the scan rate of 3 mV s^{-1} were 427, 479, 326, and 320 C g^{-1} for the W1, W2, W2, and W4 samples, respectively. For the samples M1, M2, M3, and M4, the calculated Q_s were 230, 324, 361, and 192 C g^{-1}, respectively. The specific capacities highlight that sample W2 is the best performing sample among all the tested samples, as judged from the CV results. The overall best performance of W2 may be attributed to battery-dominant materials, such as WS_2, the electrolyte ions intercalate inside the surface of electrode material to ample the redox reaction. Thus, here, W2 has enough active sights to store the electrolyte ions, which eventually enhanced its electrochemical performance. By increasing the thickness, the compact layer of WS_2 is formed, which blocks

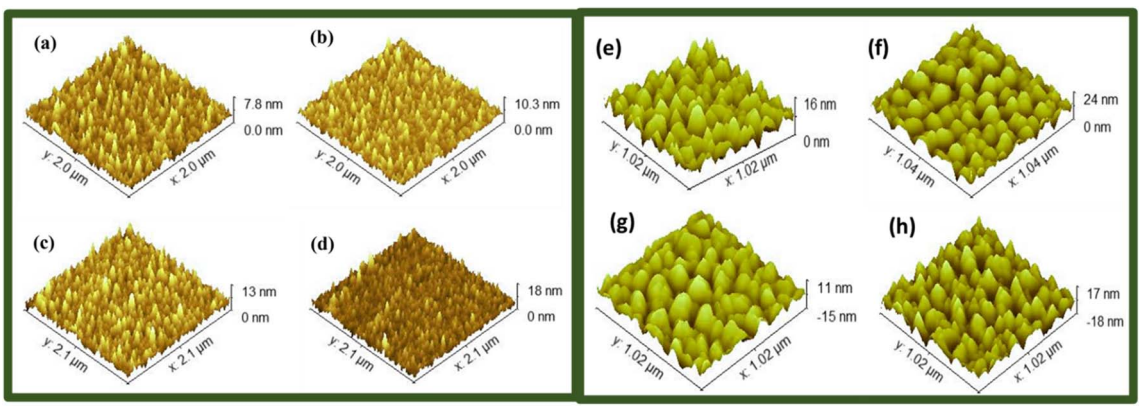

Fig. 3 AFM image of (a) W1, (b) W2, (c) W3, (d) W4, (e) M1, (f) M2, (g) M3, and (h) M4.

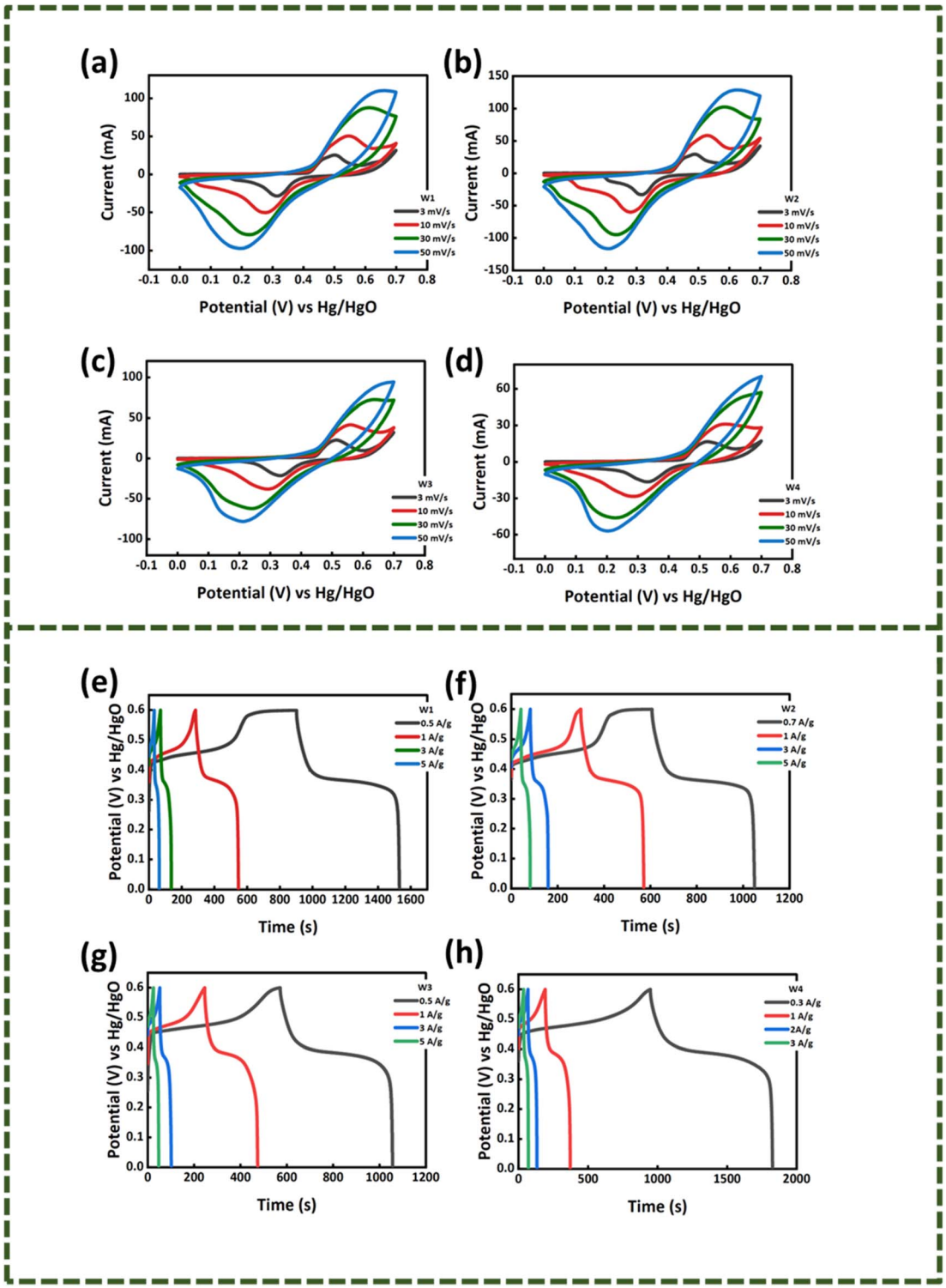

Fig. 4 Cyclic voltammograms of (a) W1, (b) W2, (c) W3, (d) W4. Galvanostatic curves of (e) W1, (f) W2, (g) W3, (h) W4.

the path of ions to intercalate inside the surface of electrode material, which may affect the energy storage performance of WS_2.

3.2.2. Galvanostatic charging discharging (GCD). After obtaining an understanding about the kinetics of the as-synthesized samples, the GCD tests were initiated in the potential window of 0–0.6 V at different current densities. The potential window was set by keeping in view the CV results as the maximum oxidation occurred in the 0.6 V region. The GCD results of WS_2 are presented in Fig. 4(e)–(h) and that of MoS_2 are

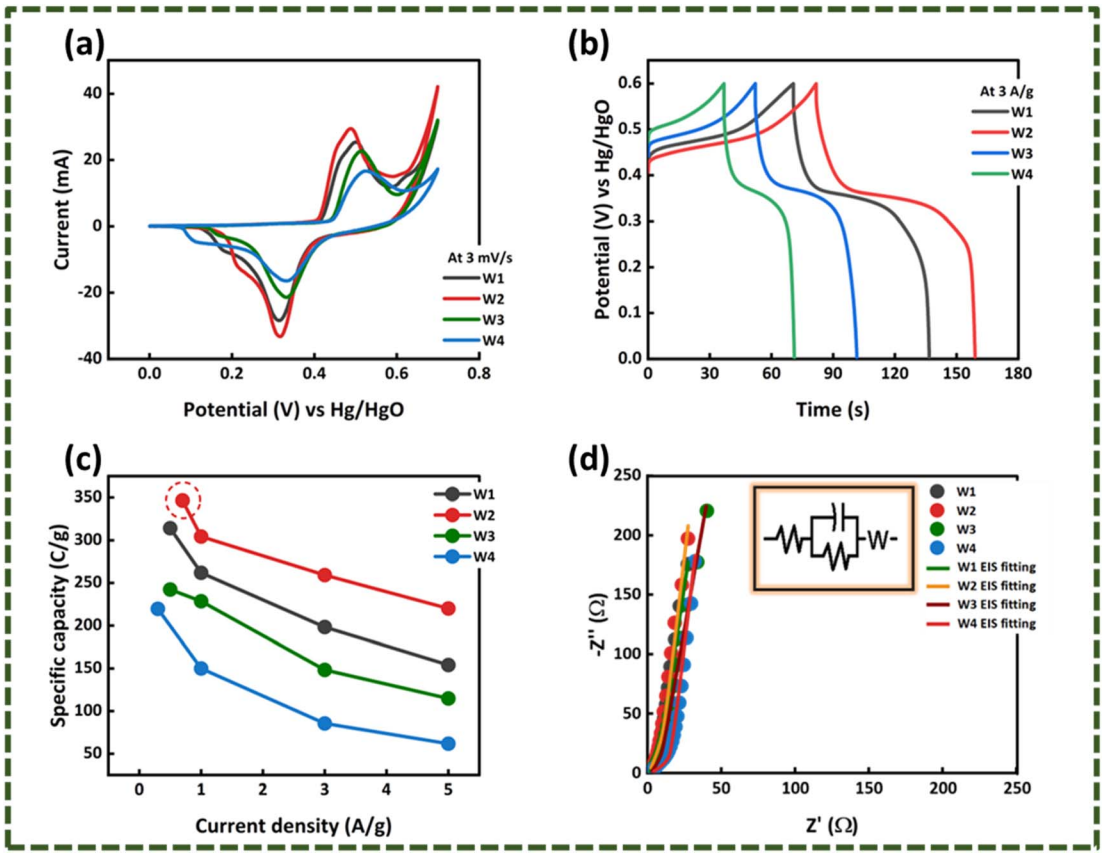

Fig. 5 Comparison of (a) cyclic voltammetry curves of the WS_2 samples. (b) GCD curves of WS_2 samples. (c) Specific capacities of WS_2 samples. (d) EIS spectrum of WS_2 samples with equivalent circuit fitting.

expressed in Fig. 6(e)–(h). The galvanostatic charging/discharging curves of all the samples are in complete accordance with cyclic voltammetry results as a hump is clearly observed in the charging-discharging curves, which shows the continuation of redox reactions. The specific capacity of sample W1–W4 and M1–M4 were calculated using eqn (4) (ref. 24)

$$Q_S = \frac{I \times \Delta t}{m} \quad (4)$$

where 'I/m' is the current density and the discharging time is specified by 'Δt'. The maximum specific capacities calculated for the samples from the GCD results were 314, 346, 242, and 219 C g^{-1} for W1, W2, W3, and W4, respectively. For M1, M2, M3, and M4, the maximum specific capacities calculated were 235, 252, 304, and 144.8 C g^{-1}, respectively. The GCD results also support the CV outcomes and shows that the same W2 is the best performing sample among all other samples, as presented in Fig. 5(c) and 7(b).

3.2.3. Electron-impedance spectroscopy (EIS). Electronic conductivity is one of the prime factors that influences the electrochemical properties of a material. To get an idea about the overall conductivity of WS_2 and MoS_2 samples, electrochemical impedance spectroscopy analysis was conducted in the range of 0.1 Hz–100 kHz. The EIS spectra of WS_2 are presented in Fig. 5(d). In the elevated frequency region, the semicircle in the EIS spectrum denotes the R_{ct} (charge transfer resistance), which is the resistance faced by ions at the electrode/electrolyte interface. In case of the WS_2 samples, negligible R_{ct} can be observed. The resistance offered to the ions, while its diffusion through the electrolyte and its interaction with the electrode is described through ESR (equivalent series resistance). The intersection of EIS spectrum with x-axis can provide the ESR value. The ESR calculated for W1, W2, W3, and W4 was 1.17, 0.88, 14.5, and 1.65 Ω, respectively. Similarly, looking at the EIS spectrum of the $MoWS_2$ sample in Fig. 7(c), it can be noticed that the samples have negligible R_{ct}. The ESR was 1.97, 2.20, 0.74, and 1.98 Ω for M1, M2, M3, and M4, respectively. The ESR also confirmed that W2 has convincing outcomes and is most favorable to be integrated in a hybrid supercapacitor assembly.

The overall best performance of WS_2 may be attributed to battery-dominant materials such as WS_2; the electrolyte ions intercalate inside the surface of electrode material to complete the redox reaction. Here, WS_2 may have enough active sites to store the electrolyte ions, which eventually enhanced its electrochemical performance. By increasing the thickness, the compact layer of WS_2 is formed, which blocks the path of ions to

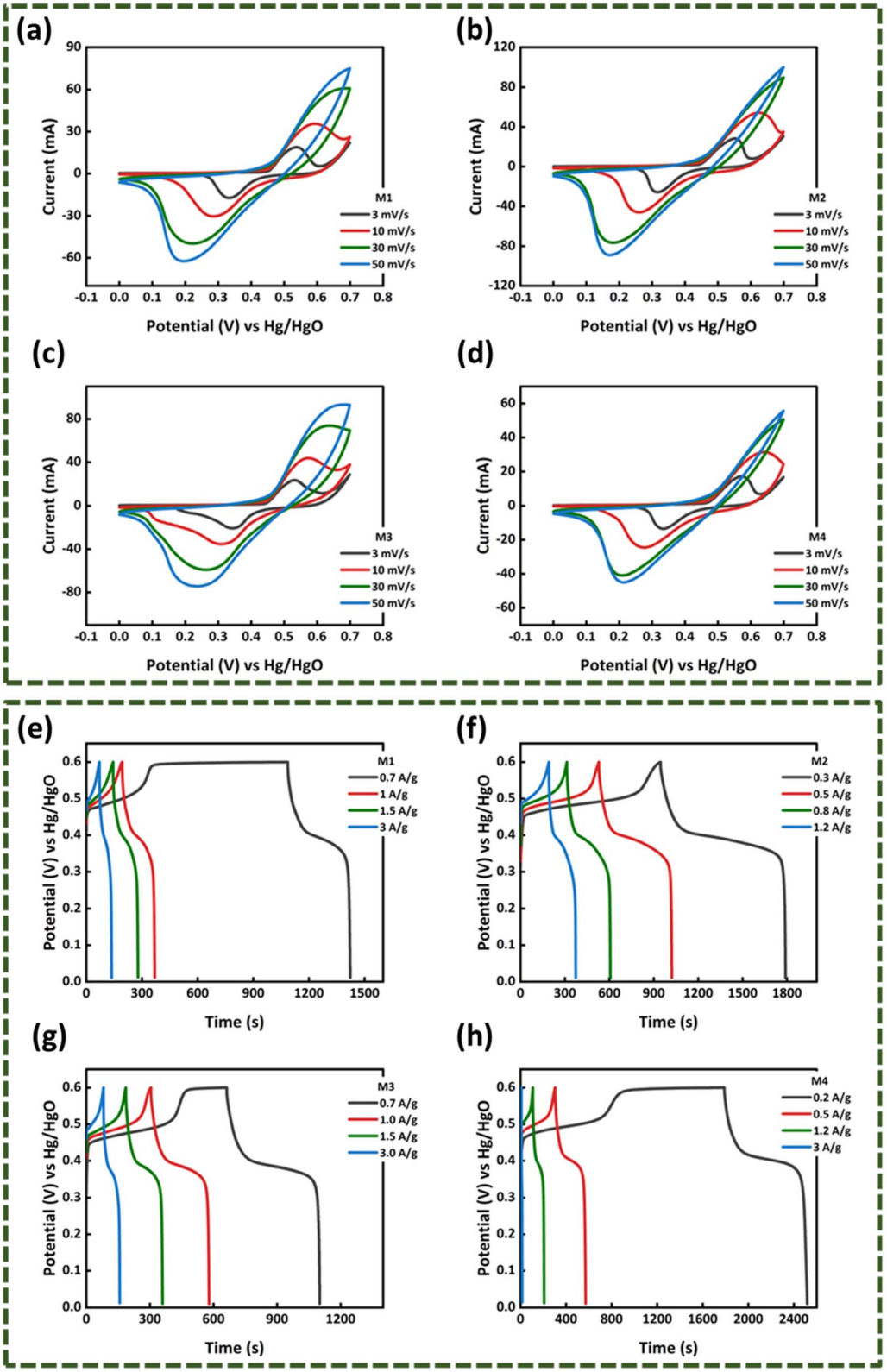

Fig. 6 Cyclic voltammograms of (a) M1, (b) M2, (c) M3, (d) M4. Galvanostatic curves of (e) M1, (f) M2, (g) M3, (h) M4.

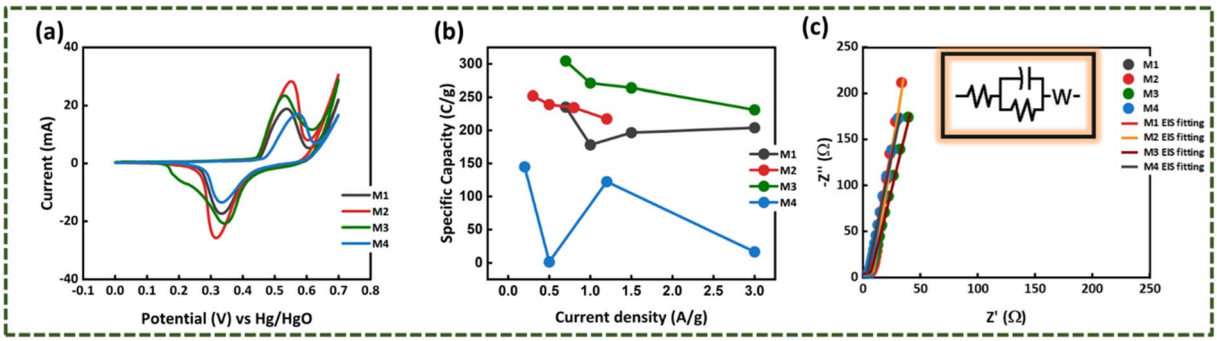

Fig. 7 Comparison of (a) the cyclic voltammetry curves of the $MoWS_2$ samples. (b) Specific capacities of $MoWS_2$ samples. (c) EIS spectrum of WS_2 samples with equivalent circuit fitting.

intercalate inside the surface of electrode material, thus affecting the energy storage performance of WS_2.

3.3. Real device fabrication

To realize the functional implication of WS_2 as a high-performance active electrode, a hybrid supercapacitive device was engineered by amalgamating activated carbon and WS_2 (sample W2) as the negative and positive electrode (WS_2//AC), respectively. The fabricated device was scrutinized for its electrochemical properties in 1 M KOH. To obtain maximum results from any hybrid device, charge balancing must be done, which was done in this current work using eqn (5).[25]

$$\frac{m_+}{m_-} = \frac{Q_{s^+} \times \Delta V_+}{C_{s^-}} \quad (5)$$

where, m_+ and m_- are the active material's mass on the anode and cathode, respectively, Q_s determines the specific capacity, ΔV is the operating voltage, and C_s is the specific capacitance.

Fig. 8(a) compares the voltammograms of both AC carbon and WS_2 in a three-electrode assembly. The working potential window of AC was in the range of 0 V to −1 V and that of WS_2 was in the range of 0–0.7 V. With that in view, the optimum potential window for the CV analysis of the fabricated device was set to 0 V–1.7 V. The cyclic voltammograms of the WS_2//AC device are displayed in Fig. 8(b), which shows that the device has symmetric peaks with the simultaneous behavior of both EDLC and battery. The symmetric curves of WS_2 are an indication that it possesses great rate capability and stability even at higher scan rates. The GCD patterns of the fabricated device are shown in Fig. 8(c). The curves represent the attributes of a hybrid device and were recorded at various current (0.9–5.0 A g^{-1}) densities between 0 V and −1.7 V. The highest discharging rate was obtained at 0.9 A g^{-1}. The Q_s calculated for WS_2//AC at 0.9 A g^{-1} was 180 C g^{-1}. Fig. 8(d) depicts the Q_s of the device extracted from the CV and GCD curves. The stability of any energy storage is an important analysis that determines whether the device can be implemented for practical purposes. In this regard, a stability test was run for 3000 GCD cycles, which showed that the fabricated device has an exceptional cyclic stability with a capacity retention of 97% (Fig. 8(f)). The energy density (E_s) and specific power (P_s) for WS_2//AC were calculated using eqn (6) and eqn (7), respectively.[26]

$$E_S = \frac{Q_s \times \Delta V}{2 \times 3.6} \quad (6)$$

$$P_S = \frac{E_s \times 3600}{\Delta t} \quad (7)$$

The hybrid device showcased a maximum energy density and P_s of values 42.5 W h kg^{-1} and 4250 W kg^{-1}, respectively (Fig. 8(e)). Electro-impedance spectroscopy was also done for the hybrid device before and after the stability test. It is visible from Fig. 9(a) that the ESR reduced after the performing stability test indicates the greater conductivity of the hybrid device.

Apart from experimental analysis, theoretical models were implied to simulate theoretical data that provided evidence that WS_2//AC has hybrid features. The power law, as mentioned in eqn (8), was used to derive the *b*-values for the asymmetric device.[27]

$$i = av^b \quad (8)$$

Where '*i*' represents the current, '*v*' is the scan rate, and '*a*' and '*b*' variable parameters. It is well known that if the *b*-value of a device is ~0.5, it bears battery-grade nature, whereas if it is ~1.0, then the capacitive nature is dominant. In the case of WS_2//AC, the *b*-values calculated were ~0.6–0.8, as can be seen in Fig. 9(b). The capacitive and diffusion contribution during the charging/discharging of the hybrid device is presented in Fig. 10(a)–(c) at 3 mV s^{-1}, 50 mV s^{-1}, and 100 mV s^{-1}, with Fig. 10(d) showing the percentage current contribution at distinct scan rates. These data were extracted using Dunn's model (eqn (9)).[28] It is obvious from the results that WS_2//AC has characteristics of a hybrid device.

$$i(V) = k_1 v + k_2 v^{\frac{1}{2}} \quad (9)$$

The decent electrochemical outcomes of WS_2 in both the three-electrode system and hybrid device puts it in great position to be further investigated for potential applications, especially for energy storage.

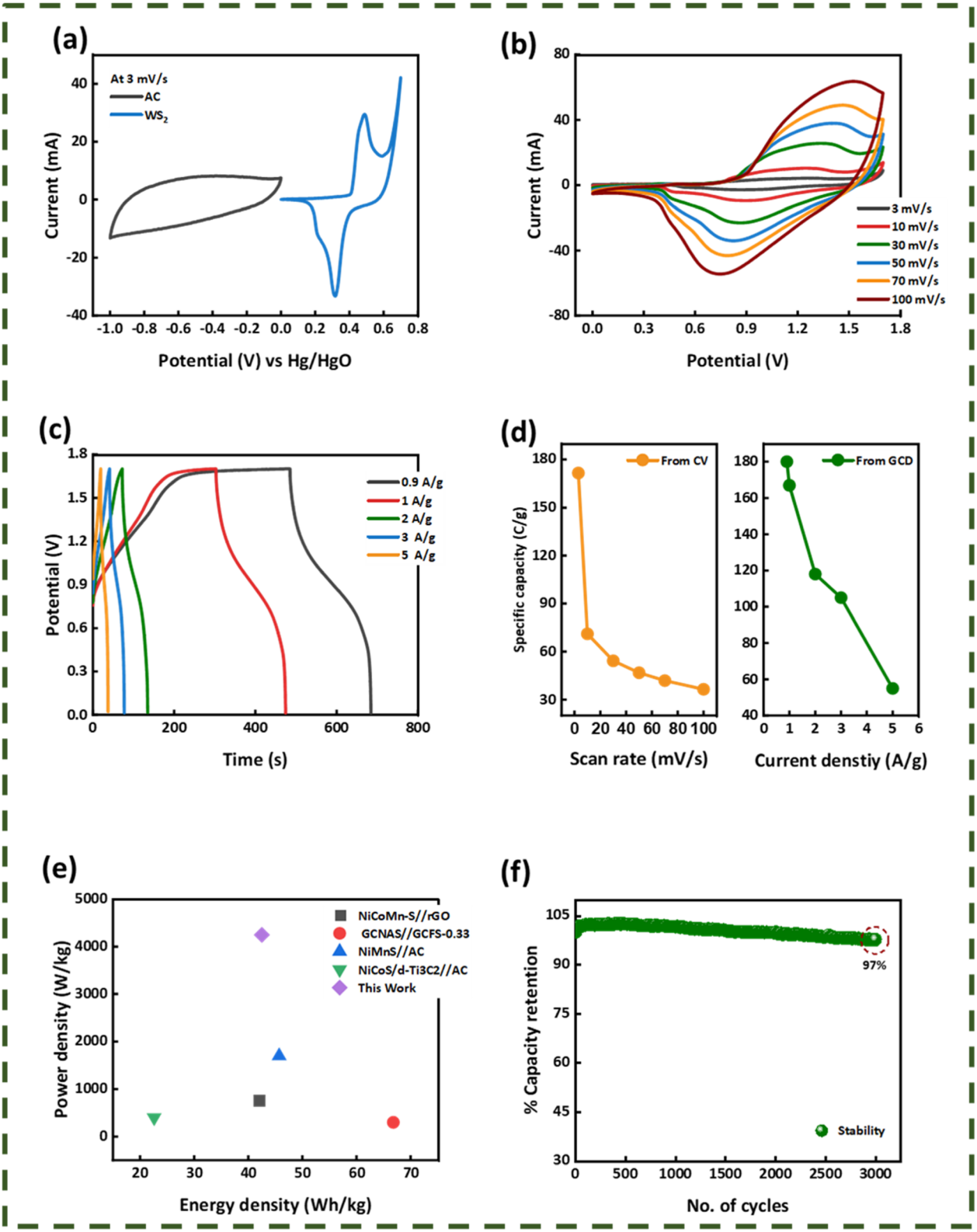

Fig. 8 (a) Comparative CV of activated carbon and WS_2(W2) at 3 mV s^{-1}. (b) CV of the WS_2//AC hybrid device. (c) GCD plot of the WS_2//AC hybrid device at various current densities. (d) Specific capacities calculated from CV and GCD for the hybrid device. (e) Energy and power density plot of WS_2//AC. (d) Stability test of the hybrid supercapacitor.

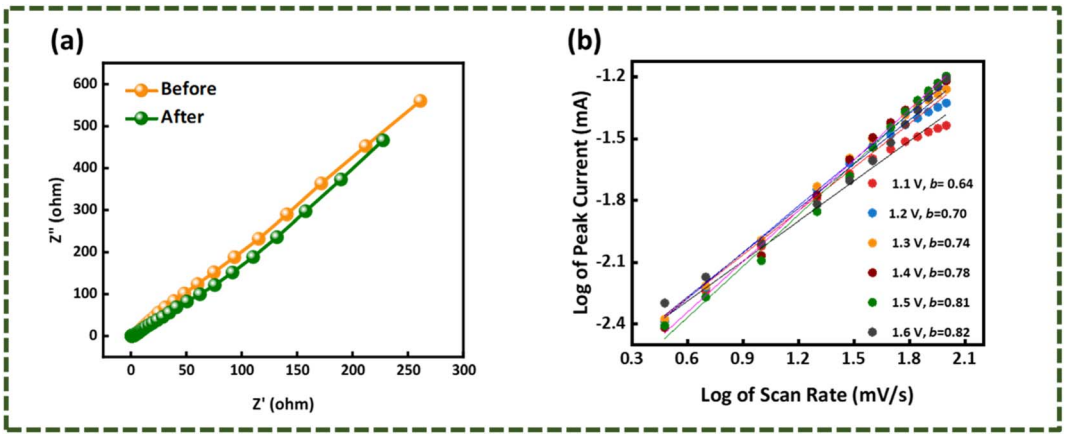

Fig. 9 (a) EIS spectrum before and after the stability test of WS_2//AC. (b) *b*-values calculated for the hybrid device.

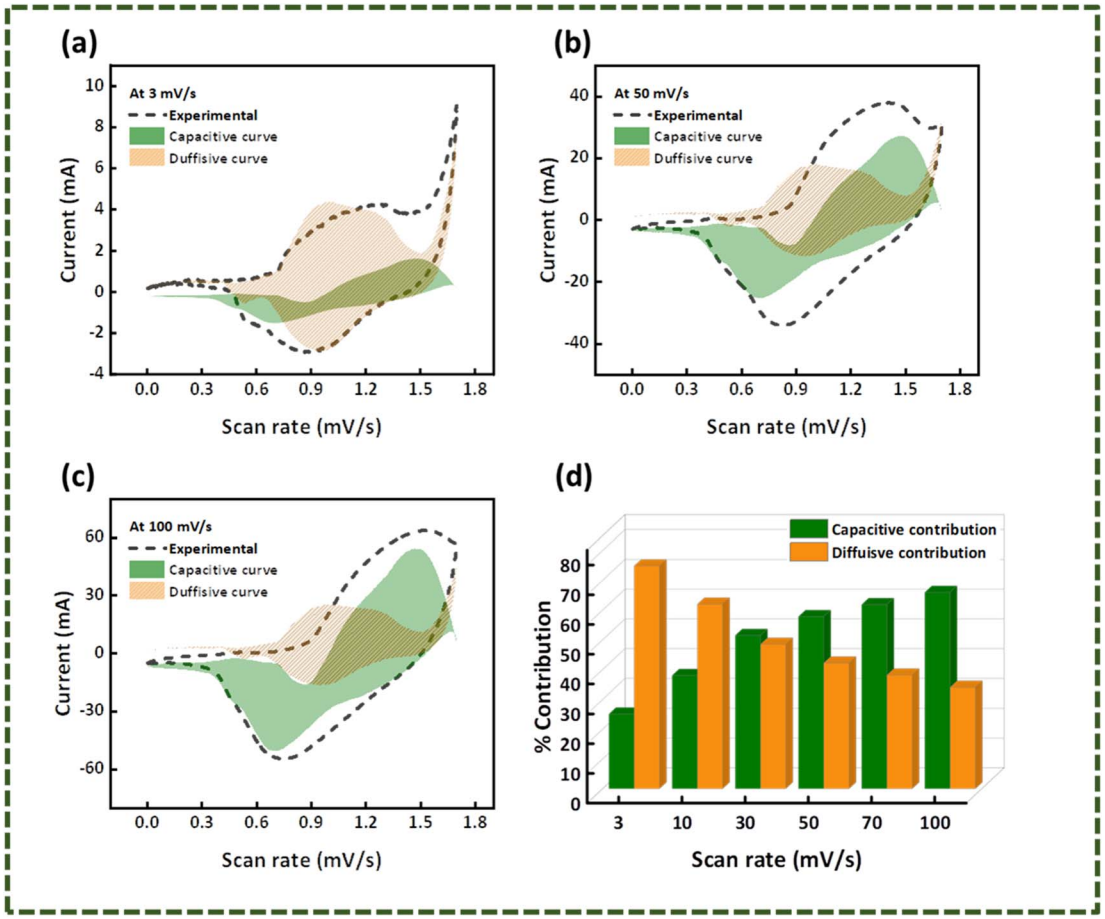

Fig. 10 Capacitive-diffusive contribution elucidated using Dunn's model at (a) 3 mV s^{-1}, (b) 50 mV s^{-1}, (c) 100 mV s^{-1}, (d) percentage capacitive-diffusive contribution at different scan rates (3–100 mV s^{-1}).

Conclusion

The electrochemical performance of binder-free WS_2 and $MoWS_2$ electrodes is studied in this analysis. WS_2 and $MoWS_2$ were magnetron-sputtered on nickel foam with different thicknesses to achieve the optimized layer. Both the materials were structurally and morphologically characterized *via* XRD, which revealed that WS_2 has two distinct structural phases, hexagonal and rhombohedral. $MoWS_2$ has a cubic structure, as is evident from the XRD pattern. The SEM images show that the sputtered material entirely covered the nickel foam. Raman and AFM studies were also performed to get insights into the

structural properties of both the materials. Electrochemical tests were initiated in the three-electrode assembly through CV, GCD, and EIS. Both WS_2 and $MoWS_2$ were identified as W2 (WS_2 sample) and performed better relative to all other samples by delivering the highest specific capacity of 479 C g^{-1}. The manufactured device assembled as W2//AC was fabricated, as characterized through electrochemical analysis. The hybrid device showed a specific capacity of 180 C g^{-1} at a current density of 0.9 A g^{-1}. Also, the device displayed a long-life cyclic stability by retaining 97% of its primary charge after 3000 charging-discharging cycles. The maximum E_s and P_s displayed by the hybrid device was 42.5 W h kg^{-1} and 4250 W kg^{-1}, respectively. In addition, the *b*-values and capacitive-diffusive contributions were elucidated using Dunn's model, which affirmed that WS_2//AC bears hybrid characteristics. The superior performance of binder-free transition-metal sulfide electrodes makes them highly desirable for future energy storage applications.

Conflicts of interest

The authors declare that they have no known competing financial interests or personal relationships that could have appeared to influence the work reported in this paper.

Acknowledgements

This work was funded by the Deanship of Scientific Research at Jouf University under grant No (DSR2022-RG-0128).

References

1 W. Liu, M.-S. Song, B. Kong and Y. Cui, *Adv. Mater.*, 2017, **29**, 1603436.
2 P. Du, Y. Dong, C. Liu, W. Wei, D. Liu and P. Liu, *J. Colloid Interface Sci.*, 2018, **518**, 57–68.
3 M. Z. Iqbal, S. R. Ali, M. M. Faisal, S. Siddique, S. Aftab and M. Alzaid, *Mater. Chem. Phys.*, 2022, **291**, 126638.
4 A. Zhamu, G. Chen, C. Liu, D. Neff, Q. Fang, Z. Yu, W. Xiong, Y. Wang, X. Wang and B. Z. Jang, *Energy Environ. Sci.*, 2012, **5**, 5701–5707.
5 Q. Guo, X. Zhao, Z. Li, B. Wang, D. Wang and G. Nie, *ACS Appl. Energy Mater.*, 2020, **3**, 2727–2736.
6 K. Le, M. Gao, W. Liu, J. Liu, Z. Wang, F. Wang, V. Murugadoss, S. Wu, T. Ding and Z. Guo, *Electrochim. Acta*, 2019, **323**, 134826.
7 M. Z. Iqbal, U. Aziz, M. W. Khan, S. Siddique, M. Alzaid and S. Aftab, *J. Electroanal. Chem.*, 2022, **924**, 116868.
8 Q. Zhou, Y. Gong and K. Tao, *Electrochim. Acta*, 2019, **320**, 134582.
9 Q. Lu, J. G. Chen and J. Q. Xiao, *Angew. Chem., Int. Ed.*, 2013, **52**, 1882–1889.
10 D. Wang, Y. Wang, Z. Fu, Y. Xu, L.-X. Yang, F. Wang, X. Guo, W. Sun and Z.-L. Yang, *ACS Appl. Mater. Interfaces*, 2021, **13**, 34507–34517.
11 M. Z. Iqbal and J. Khan, *Electrochim. Acta*, 2021, **368**, 137519.
12 Z. Xu, Z. Zhang, H. Yin, S. Hou, H. Lin, J. Zhou and S. Zhuo, *RSC Adv.*, 2020, **10**, 3122–3129.
13 N. Gupta, R. K. Sahu, T. Mishra and P. Bhattacharya, *J. Mater. Chem. A*, 2022, **10**, 15794–15810.
14 A. Agarwal and B. R. Sankapal, *J. Mater. Chem. A*, 2021, **9**, 20241–20276.
15 Y. Sun, T. Zhang, C. Li, K. Xu and Y. Li, *J. Mater. Chem. A*, 2020, **8**, 13415–13436.
16 M. Z. Iqbal, U. Abbasi and S. Alam, *Int. J. Energy Res.*, 2022, **46**, 3906–3938.
17 S. Nandhini, A. Juliet Christina Mary and G. Muralidharan, *Appl. Surf. Sci.*, 2018, **449**, 485–491.
18 Y. Yang, S. Li, F. Liu, J. Wen, N. Zhang, S. Wang and K. Liu, *Nanotechnology*, 2018, **29**, 455401.
19 H. Heydari, S. E. Moosavifard, S. Elyasi and M. Shahraki, *Appl. Surf. Sci.*, 2017, **394**, 425–430.
20 W. Chen, X. Yu, Z. Zhao, S. Ji and L. Feng, *Electrochim. Acta*, 2019, **298**, 313–320.
21 V. V. Mohan, M. Manuraj, P. M. Anjana and R. B. Rakhi, *Energy Techol.*, 2022, **10**, 2100976.
22 M. Z. Iqbal, S. Siddique and Z. Abideen, *Carbon*, 2017, **123**, 168–173.
23 Y. Luo, K. Gu, T. Yang and M. Zhang, *J. Energy Storage*, 2019, **21**, 362–369.
24 M. Z. Iqbal, M. W. Khan, M. Shaheen, S. Siddique, S. Aftab, M. Alzaid and M. J. Iqbal, *J. Energy Storage*, 2022, **55**, 105418.
25 D. M. Sayed, M. M. Taha, L. G. Ghanem, M. S. El-Deab and N. K. Allam, *J. Power Sources*, 2020, **480**, 229152.
26 S. Dai, B. Zhao, C. Qu, D. Chen, D. Dang, B. Song, B. M. deGlee, J. Fu, C. Hu, C.-P. Wong and M. Liu, *Nano Energy*, 2017, **33**, 522–531.
27 L. Fan, K. Lin, J. Wang, R. Ma and B. Lu, *Adv. Mater.*, 2018, **30**, 1800804.
28 J. Wang, J. Polleux, J. Lim and B. Dunn, *J. Phys. Chem. C*, 2007, **111**, 14925–14931.